Spectrochimica Acta Part B: Atomic Spectroscopy 210 (2023) 106806

Contents lists available at ScienceDirect

Spectrochimica Acta Part B: Atomic Spectroscopy

journal homepage: www.elsevier.com/locate/sab

3D printed imaging apertures for MicroPattern gas detector based full field of view X-ray fluorescence spectrometers

P.M.S. Carvalho [a,*], F.D. Leite [a], Gil Tavares [a], P.M.M. Correia [a], J.M.M. Oliveira [b,c], J.F.C.A. Veloso [a], A.L.M. Silva [a]

[a] Institute for Nanostructures, Nanomodelling, and Nanofabrication (i3N), Department of Physics, University of Aveiro, Campus Universitário de Santiago, 3810-193 Aveiro, Portugal
[b] CICECO – Aveiro Institute of Materials, University of Aveiro, Campus Universitário de Santiago, 3810-193 Aveiro, Portugal
[c] Escola Superior de Design, Gestão e Tecnologias da Produção de Aveiro-Norte (ESAN), Universidade de Aveiro, Estrada do Cercal 449, 3720-509 Santiago de Riba-Ul, Oliveira de Azeméis, Portugal

ARTICLE INFO

Keywords:
Full-field XRF imaging
3D printing
Multi-hole collimator
Sensitivity
Position resolution

ABSTRACT

Additive Manufacturing, commonly referred as 3D printing, opened a new way to promptly produce cost-effective imaging apertures based on high-density materials, to be used in x-ray imaging systems, such as MicroPattern Gas Detector (MPGD) based Full Field X-ray Fluorescence (FF-XRF) spectrometers. These provide energy and spatially resolved information, allowing the mapping of large area samples. Traditionally, image formation is accomplished with pinhole apertures, devices of easy manufacturing that lead to sub-micrometre position resolution values. However, the sensitivity of the imaging system is severely hampered. To surpass this issue, alternative optical components, such as parallel multi-hole collimators, can be used.

In this work, 3D printed multi-hole collimators with different geometries and material compositions are presented and applied to a FF-XRF spectrometer based on the 2D-THCOBRA gas detector. The system's performance parameters with different collimators, namely, relative sensitivity and position resolution, were experimentally determined and compared with the ones obtained with pinhole-based setups. The FF-XRF spectrometer was also simulated, to understand how different collimator geometries affect sensitivity and position resolution.

1. Introduction

X-ray Fluorescence (XRF) is based on the irradiation of a sample with sufficiently energetic photons to induce the emission of characteristic x-rays, that are detected and analysed so that a sample's elemental content can be identified and quantified. Common XRF spectrometers rely on energy sensitive detectors, e.g., solid state detectors, for photon detection. Yet, position sensitive detectors, namely MicroPattern Gas Detectors (MPGD), are an advantageous alternative as they allow mapping the elemental distribution throughout a large sample's surface, without scanning mechanisms [1].

MPGDs such as the 2D Micro-Hole and Strip Plate (2D-MHSP) or the 2D Thick COBRA (2D-THCOBRA) have already been successfully applied in full-field XRF (FF-XRF) imaging spectrometers, providing energy and spatially resolved information. For the last decade, such systems have been applied in biomedical [2] and cultural heritage [3,4] studies. Recently, P. M. S. Carvalho et al. [5] employed a full-field XRF spectrometer based on a large area 2D-THCOBRA detector to map pigments in handmade decorative tiles and to evaluate the restoration of a late XIX – early XX century Portuguese faience piece. The spectrometer relied on a 1 mm lead pinhole for image formation; and each elemental mapping lasted between 59 min and 100 min for areas around 5×5 cm^2. The same system was used by F. D. Leite et al. [6] to determine heavy metal accumulation in contaminated Zebrafish. In this case, a 500 μm pinhole aperture was used to map the distribution of Mn, Se, and Pb within three different animal samples (lengths ranging from 25 to 35 mm) – acquisition times varied between 100 and 120 min.

These imaging spectrometers are characterised by their simple and low-cost instrumentation, requiring only a simple and inexpensive optical component, of easy manufacturing, for image formation – a pinhole aperture. It is merely a small hole in a piece of a high-density and high atomic number material (e.g., lead or tungsten) that provides a cone-beam image incident into the detector with the focus point at the pinhole, enabling image magnification by varying the ratio between the

* Corresponding author.
E-mail address: pmcarvalho@ua.pt (P.M.S. Carvalho).

https://doi.org/10.1016/j.sab.2023.106806
Received 6 July 2023; Received in revised form 5 October 2023; Accepted 9 October 2023
Available online 13 October 2023

pinhole-to-detector distance and the object-to-pinhole distance [7–9]. Thus, spatially resolved images with sub-millimetre resolution values are obtained, albeit at the expense of decreased system sensitivity and increased acquisition times.

The spatial resolution, or position resolution, of an imaging system with a pinhole aperture ($R_{S,P}$) is given by Eq. (1) [10]:

$$R_{S,P} = \sqrt{\lambda_g^2 + \lambda_i^2} = \sqrt{d^2\left(1+\frac{1}{M}\right)^2 + \frac{FWHM_i^2}{M^2}} \quad (1)$$

where λ_g is the geometric resolution of an ideal pinhole aperture; λ_i is the detector's intrinsic position resolution, related to the Full-Width Half Maximum of the detector's response, $FWHM_i$; d is the diameter of the pinhole aperture; and M is the magnification induced by the pinhole.

From Eq. (1), the spatial resolution can be improved by decreasing the diameter of the pinhole aperture. However, it quadratically reduces the sensitivity of the system (S_P), as highlighted by Eq. (2) [10]:

$$S_P = \frac{d^2 sin^3\theta}{16h^2} \quad (2)$$

where θ is the angle of incidence measured from the plane of the pinhole, and h is the distance from the source to the pinhole plane.

To overcome sensitivity constraints, parallel multi-hole collimators are considered as an alternative to pinhole apertures. These structures, represented in Fig. 1, are also made of high-density and high atomic number materials, and have closely packed holes (usually hexagonally shaped) through which the desired photons pass. The holes are arranged in a honeycomb pattern and are separated by walls, the septa [9,11].

The geometric resolution of a multi-hole collimator (λ_C), given by Eq. (3), is affected by the hole's diameter (d), the depth of the collimator (a), and by the perpendicular distance from the object to the detector (h) [11]:

$$\lambda_C = d\frac{a+h}{a_{eff}(E)} \quad (3)$$

where $a_{eff}(E)$ is the collimator's effective thickness, adjusted for penetration effects, following:

$$a_{eff}(E) = a - \frac{2}{\mu(E)} \quad (4)$$

with $\mu(E)$ being the attenuation coefficient of the collimator's material, and E, the energy of the transmitted photon.

Sensitivity for a collimator with hexagonal holes (S_C) can be determined through Eq. (5) [11]:

$$S_C = \frac{\sqrt{3}}{8\pi}\frac{d^2}{a_{eff}^2(E)}\frac{d^2}{(d+t)^2} \quad (5)$$

where t is the thickness of the septa.

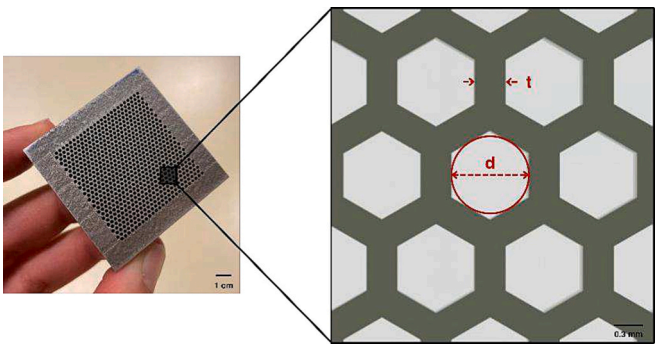

Fig. 1. Geometry of a parallel multi-hole collimator with hexagonal holes, highlighting the hole diameter (d), and septa thickness (t).

From Eqs. (3) to (5), it is expected that the collimator material affects the performance of the imaging systems. For example, fewer photons can penetrate and pass through a material with higher attenuation coefficient, thus reducing sensitivity. At the same time, position resolution can improve, as photons travelling in directions other than the collimator holes are likely absorbed.

The manufacture of an ideal collimator, that provides optimised position resolution and sensitivity, may be challenging. Traditionally, multi-hole collimators are produced through the stamping and stacking of lead foils or by the casting of molten lead, but it limits the hole diameter to a minimum of 1.2 mm and septa thickness to 150 μm [11], which may hinder applications such as small animal x-ray imaging. Desai et al. [12] presented photochemical etching of stacked tungsten foils as an alternative to produce collimators with finer features, having reviewed, for example, a high resolution parallel-hole tungsten collimator with 260 μm wide cells, arrayed on a 380 μm pitch. Still, this technique requires the precise alignment of the foils and precision is limited by the foil thickness. Another option for producing precise and defectless collimators is x-ray or optical lithography combined with electroforming – copper and gold collimators with 25 μm thick septa were reported [13,14].

Recently, additive manufacturing opened a new way to produce complex X-ray collimators from a 3D computer aided design (CAD) file. It is a set of processes that allow the joining of materials to make parts from 3D model data, usually layer upon layer, in precise geometric shapes [15,16]. 3D printing has already been used, for example, to produce stainless steel metal collimators with 250 μm thick septa, for compact gamma probes. Position resolution values below 5.6 mm FWHM and efficiency of 44% were reported [17]. Deprez et al. [18] reported the manufacture of a multi-pinhole collimator, with twenty loft-holes of 500 μm diameter, for dual-modality SPECT-MR imaging.

From the different additive manufacturing techniques, we highlight Fused Filament Fabrication (FFF) and Selective Laser Melting (SLM). With FFF, a material is melted and deposited through a nozzle tracing each layer's geometry [19]; SLM works by selectively melting a powder, with a high intensity laser, following a designed geometry [20]. We used these processes to manufacture different parallel multi-hole collimators, with different metal compositions and geometries, that were applied to a FF-XRF spectrometer based on the 2D-THCOBRA. The sensitivity of the system and the position resolution were determined for each setup and compared with results obtained with pinhole apertures.

2. Materials and methods

2.1. Full-field XRF spectrometer

A full-field XRF imaging spectrometer based on a 2D-THCOBRA detector was used for this study. The spectrometer is composed of a Mo X-ray tube (5000 Apogee series, Oxford Instruments) for sample irradiation, a large area 2D-THCOBRA detector operating in a continuous flow of Ne/5%CH_4, and an optical component for image formation. These components are arranged in a planar geometry, with the X-ray tube irradiating the sample at a 45° angle.

The main component of this system is the 2D-THCOBRA detector, a micropattern gas detector enabling the determination of the energy (energy resolution of approximately 1 keV FWHM@5.9 keV) and the position of interaction of incident X-ray photons (intrinsic imaging capability and resolution under 400 μm FWHM) [4,5,21]. Schematical representations of the spectrometer and a picture of the 2D-THCOBRA detector are shown in Fig. 2. More detailed descriptions of the FF-XRF spectrometer and the detector are presented in previous works, such as Carvalho et al. [5] and Carramate et al. [21].

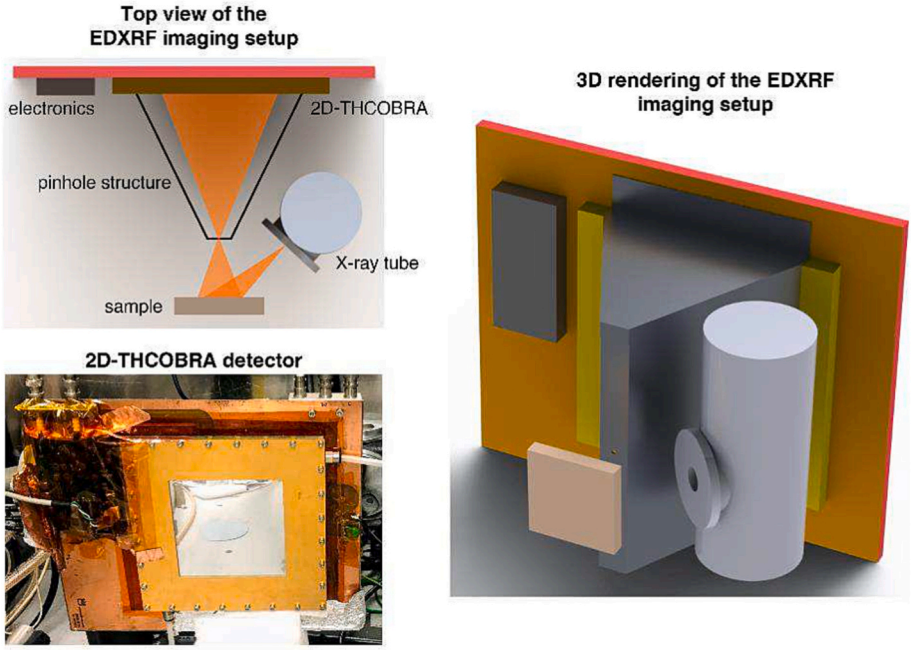

Fig. 2. The FF-XRF spectrometer based on a 2D-THCOBRA detector. Top view and rendering of the setup with a pinhole aperture, and picture of the detector (from the top left, clockwise). Image reproduced from [8].

2.1.1. Optical components

2.1.1.1. Pinhole aperture. For the purposes of this study, three lead pinhole apertures with different hole diameters — 0.3 mm, 0.5 mm, and 1 mm — were used. They were placed 6 cm away from the detector's window, coupled to a lead covered stainless steel structure.

2.1.1.2. Parallel multi-hole collimators. Five different parallel multi-hole collimator prototypes, shown in Fig. 3, were investigated. They were coupled to the detector's window, that was partially covered with a lead foil to ensure that only the photons directed towards a 30×30 mm^2 active area were detected.

Prototypes A and B were produced via FFF, using copper and tungsten-based filaments, respectively. Both have 1 mm round holes, 500 μm septa, 1 cm depth, and a 30×30 mm^2 active area. Prototype C is an aperture commonly used in gamma cameras, made of lead. It has a pattern of hexagonal holes with a 2 mm diameter, 200 μm thick septa, 4 cm depth, and a 56×60 mm^2 active area. Finally, prototypes D and E were produced via SLM using maraging steel. Both have hexagonal holes, with diameters of 1 mm (D) and 0.5 mm (E), 300 μm septa, 1.5 cm depth, and 30×30 mm^2 active areas. The characteristics of each multi-hole collimator are summarized in Table 1.

For the FFF technology, filaments with a diameter of 2.85 mm of PLA/Cu and PLA/W composites from The Virtual Foundry were used. The filaments present 88% of Cu and 92.7% of W, respectively, and a standard 3D printer with the E3D extruder was used to print them. Printing tests were performed using the following operating parameters: 0.6 mm nozzle diameter, 210°C nozzle temperature, 0% fan speed, 50°C bed temperature, 1800 mm/*min* printing speed. The infill pattern used was 45° with 100% of infill, with a layer height of 0.2 mm. The printed parts were not subject to any baking process, and therefore their structural integrity is maintained (e.g., no shrinkage of the parts) and PLA remains in their compositions. This affects the attenuation coefficient of each collimator, slightly reducing it, and thus increasing the effective depth $a_{\text{eff}}(E)$.

For the SLM process, a commercial maraging steel 18Ni300 (Renishaw, UK) gas atomized powder with nearly spherical particles with $D50 = 35$ μm and $D90 = 48$ μm was used. The 18Ni300 has the following chemical composition (%wt): 67.44 Fe, 17.58 Ni, 8.86 Co, 5.25 Mo, 0.5 Ti, and 0.37 Si. An AM 500Q SLM machine (Renishaw, UK) equipped with four ytterbium fibre lasers and a reduced build volume (RBV) of $78 \times 78 \times 55$ mm^3 was used. To reduce the risk of distortion and defects, and supported by a previous work [23], the following set of parameters were used: 300 W laser power, 1000 mm/s scanning speed, 60 μm layer thickness, 20 μm point distance, and 0.09 mm hatch distance.

2.1.2. Sample description

Metal samples, shown in Fig. 4, were used to investigate the performance of the FF-XRF spectrometer with the different optical components, namely iron and copper squares ($\cong 15 \times 15$ mm^2), and a steel washer (outer diameter = 12 mm, inner diameter = 6 mm), mainly composed of Fe.

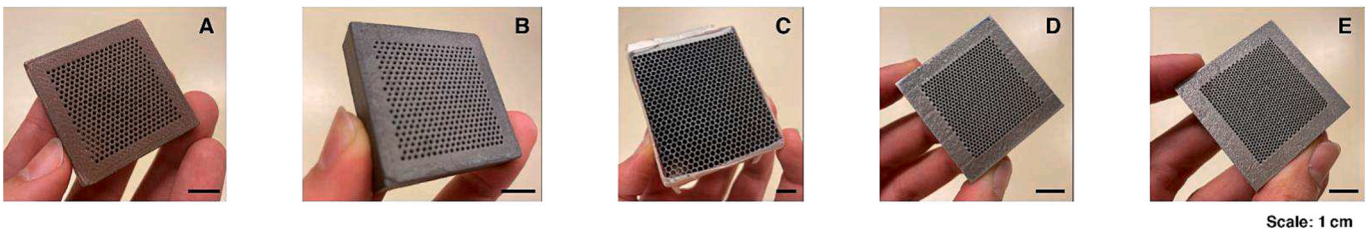

Fig. 3. Parallel Multi-Hole Collimators: A – Copper, B – Tungsten, C – Lead, D and E – Maraging Steel.

Table 1
Characteristics of the different multi-hole collimators: material, mass attenuation coefficient (μ/ρ) at 6.4 keV, production technique, hole diameter (d), hole shape, septa thickness (t), collimator depth (a), and active area (A). Mass attenuation coefficients are derived from NIST Standard Reference Database 126 [22].

–	Material	μ/ρ (cm^2/g) at 6.4 keV	Production technique	Geometry				
				d (mm)	Hole shape	t (mm)	a (mm)	A (mm^2)
A	PLA/Cu	88.70	FFF	1	Round	0.5	10	30 × 30
B	PLA/W	277.54						
C	Pb	382.70	–	2	Hexagonal	0.2	40	55 × 60
D	Maraging steel	89.21	SLM	1	Hexagonal	0.3	15	30 × 30
E				0.5				

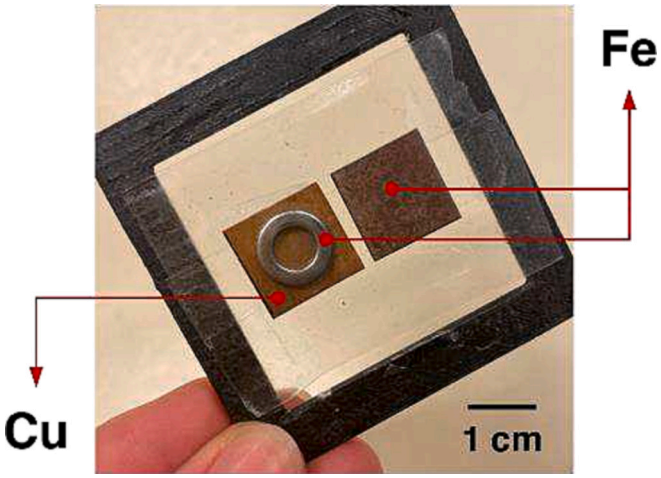

Fig. 4. Fe and Cu samples.

2.2. Assessment of performance parameters – sensitivity and position resolution

The performance of the full-field XRF imaging system was evaluated in terms of sensitivity and position resolution. The sensitivity measures the ratio of emitted versus detected photons; and the position resolution gives a measure of the minimum size of an object that can be discriminated and seen in the obtained image.

In this work, both parameters were determined from XRF analyses of a Fe square sample. The sensitivity was calculated from the number of detected photons, i.e., the total number of spectrum counts. We presented the sensitivity of each optical component relatively to the one with fewer detected photons ($S = 1$). The position resolution was determined from the obtained image, that gives us the intensity profile of the incident radiation, i.e., the Edge Spread Function (ESF). A sigmoid function was fitted to the ESF, and the Line Spread Function (LSF) was computed from its first derivative. The position resolution value is determined from the LSF's FWHM, as represented in Fig. 5. The associated uncertainty is calculated from the 95% confidence interval of the parameters of the fit to the LSF.

2.2.1. Simulation with GATE

Computer simulations of the FF-XRF spectrometer with different optical components were carried out to understand the contribution of the different geometry parameters on the system's sensitivity and position resolution.

The experimental setup described in Section 2.1 was simulated using GATE, an advanced opensource software based on Geant4, dedicated to numerical simulations for medical imaging and radiotherapy [24]. Three components of the experimental setup were simulated – a 4 × 4 × 1 cm^3 sensitive gas volume representing the detector, an optical component (designed with CAD software), and a 5 × 5 mm^2 Fe sample emitting 10^8 photons, within a 20 × 20 × 20 cm^3 air volume (World). Pinhole apertures of different diameters (250 μm, 500 μm, and 1 mm) were designed as well as a default lead parallel multi-hole collimator (1 mm hole diameter, 300 μm septa, and 1.5 cm depth), whose geometry was varied for each simulation. The simulation process is represented in Fig. 6.

2.2.2. Experimental

For the experimental determination of the system's relative sensitivity and position resolution, EDXRF analyses of a Fe square sample were performed with the different optical components. The acquisitions were performed under the same conditions – the X-ray tube was operated at 21 kV and 750 μA, and each acquisition lasted 20 *min*. The positioning of the sample was also taken into account. When using the pinhole apertures, the sample was placed so that $M = 1$ – the pinhole is placed 6 cm away from the detector, and the sample, 6 cm away from the pinhole. When multi-hole collimators were used, the sample was placed as close as possible to the collimator and the detector, 15 mm away from the collimator, to prevent worsening the position resolution.

Each analysis yielded an intensity map and a spectrum, through which the position resolution and the sensitivity were calculated, respectively, as represented in Fig. 7.

3. Results and discussion

3.1. Simulation

The behaviour of sensitivity and position resolution with pinhole apertures and parallel multi-hole collimators of different geometries was

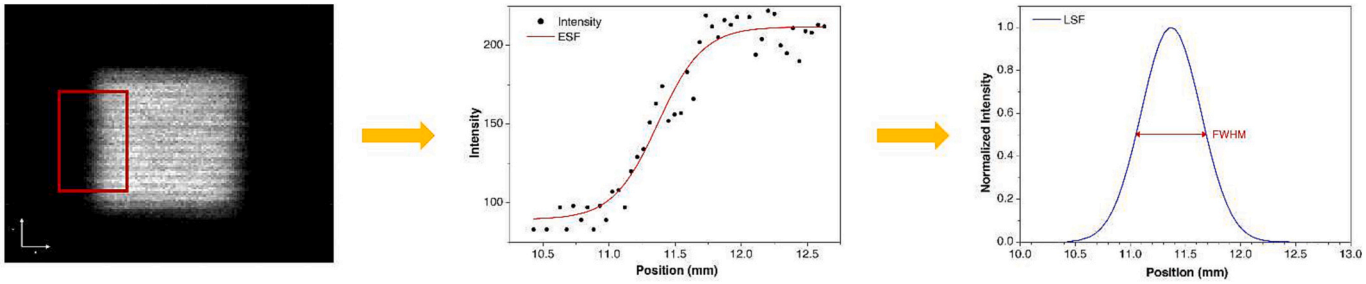

Fig. 5. Determination of the system's position resolution. Left to right: XRF image of a Fe sample and selected area; corresponding intensity profile and ESF; LSF and FWHM.

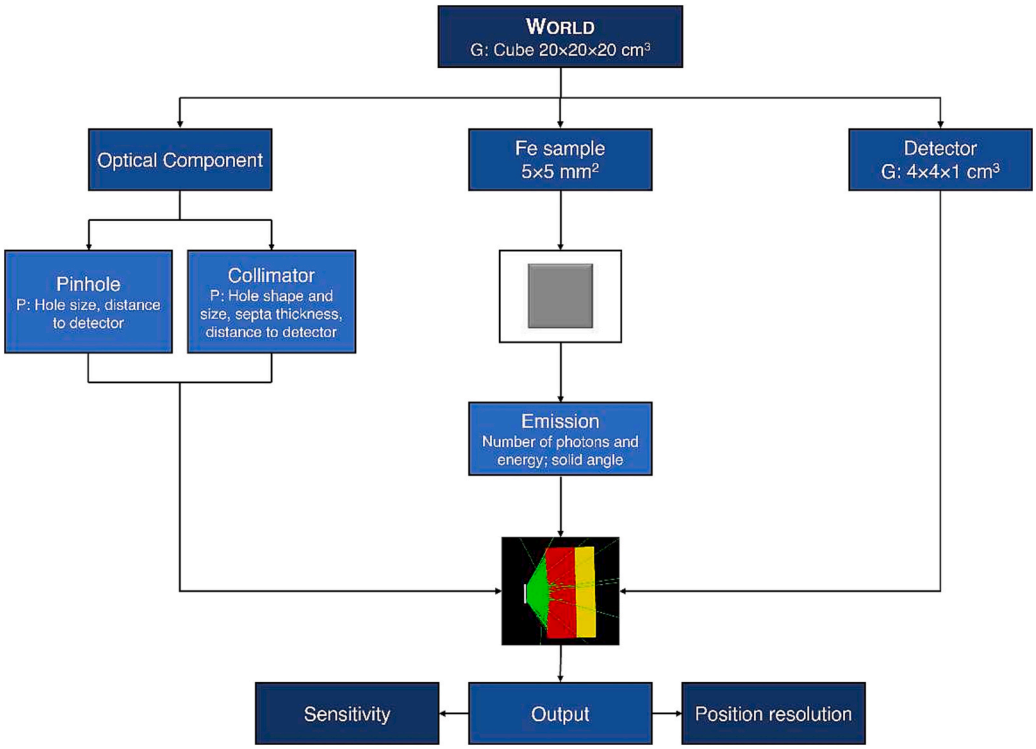

Fig. 6. GATE simulation process (G – geometry, and P – parameters.).

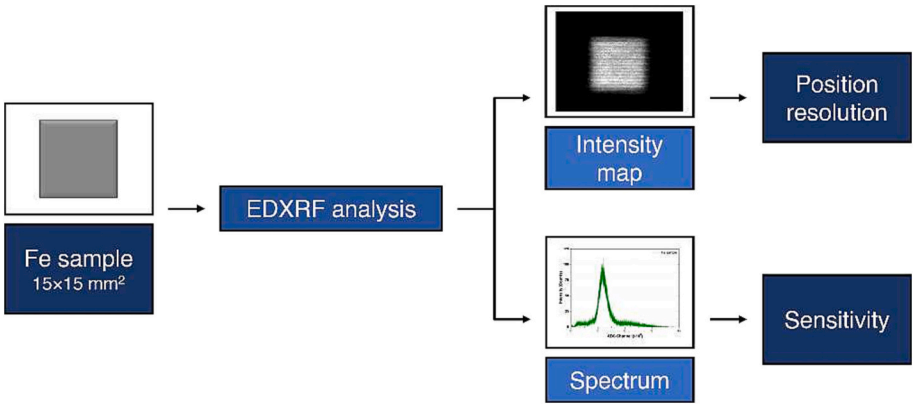

Fig. 7. Representation of the experimental determination of the system's position resolution and sensitivity.

evaluated. Results from the conducted simulations are presented in this section.

Fig. 8 a) shows the relative sensitivity and the geometric position resolution values obtained for parallel multi-hole collimators with different hole shapes – hexagon inscribed to a 1 mm diameter circular hole (HI), 1 mm circular hole (C), and hexagon circumscribed to a 1 mm diameter circular hole (HC). The variation of the parameters' values is small: the sensitivity only improves approximately 1.4 relatively to the lowest value, obtained with the HI geometry; and the resolution varies between 1.21 ± 0.02 mm and 1.27 ± 0.03 mm. These results allowed us to conclude that the hole shape does not influence the performance of the collimator. Conversely, the thickness of the septa does – as shown in Fig. 8 b), thicker septa will lead to lower sensitivities and worse position resolution. The former goes up to 2.7 with the thinner septa; and the latter varies between 1.38 ± 0.03 mm for the 100 μm thick septa, and 2.43 ± 0.05 mm for the 800 μm thick septa.

Regarding the influence of the collimator depth on the performance, it is clear from Fig. 8 c) that the deeper the collimator, the lower the sensitivity and the better the position resolution. For example, a 2.5 cm deep collimator will yield the best position resolution value, 1.24 ± 0.03 mm, at the expense of sensitivity.

Finally, Fig. 8 d) shows the relative sensitivity and position resolution as a function of the sample to collimator distance. In this case, the variation of the relative sensitivity is not significant, contrary to the position resolution. It varies between 1.07 ± 0.02 mm mm and 3.68 ± 0.08 mm, degrading with increasing distance, as expected from Eq. (3).

Finally, the relative sensitivity and position resolution were compared between different pinhole apertures and multi-hole collimators. The results, shown in Fig. 9, highlight how the increase in diameter leads to higher relative sensitivity and worse position resolution, as expected from the equations described in Section 1. The sensitivity reaches its highest value with the collimator with 1.5 mm holes – 37 times higher than the lowest value obtained with the 0.25 mm pinhole aperture. Regarding the position resolution, it varies between 0.41 ± 0.01 mm and 2.12 ± 0.04 mm, for the smallest pinhole aperture and the

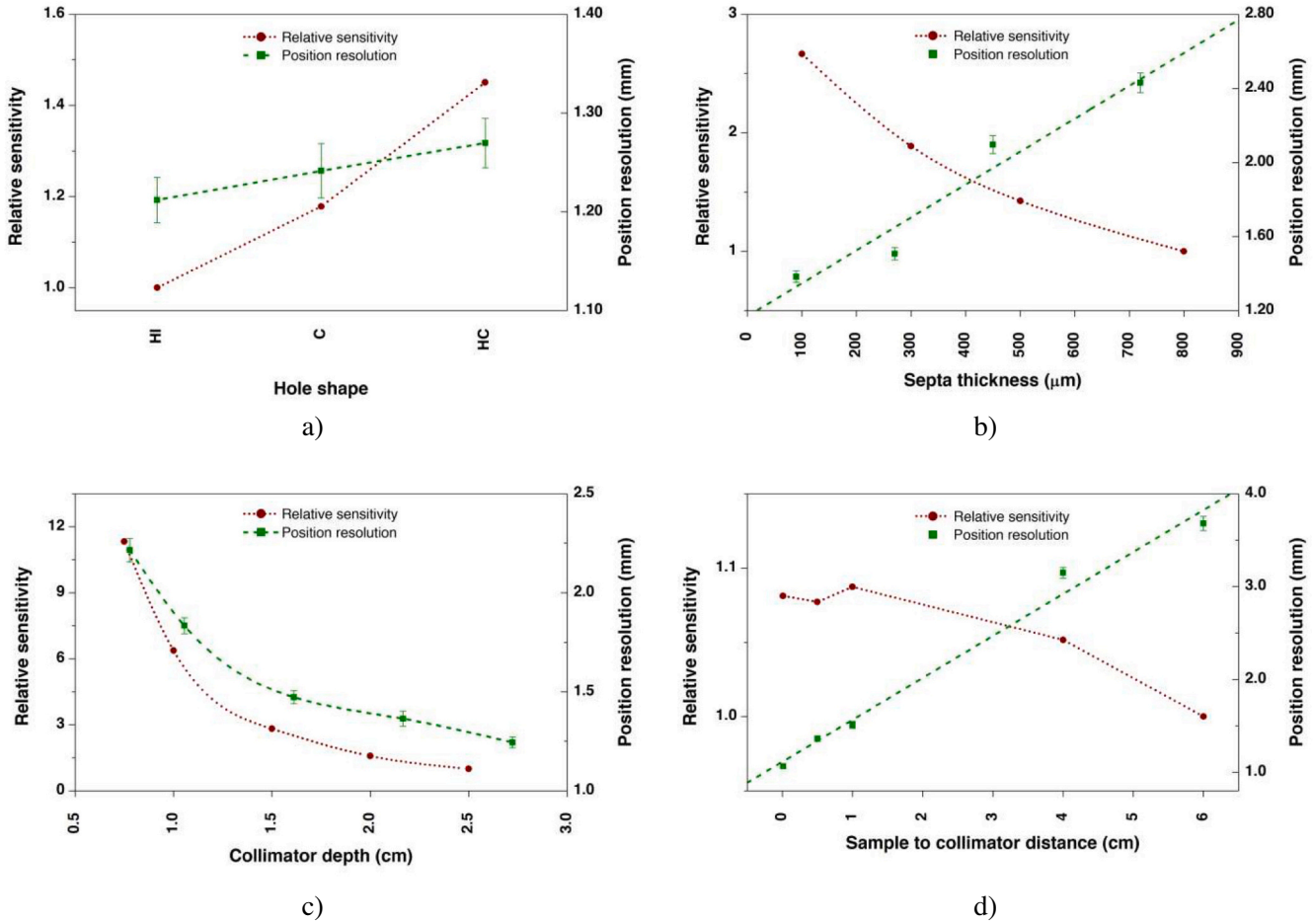

Fig. 8. Relative sensitivity and position resolution for multi-hole collimators with different geometries: a) different hole shapes – inscribed hexagon (HI), circular (C), and circumscribed hexagon (HC); b) septa thickness ranging from 100 μm to 800 μm; c) collimator depth ranging from 0.75 cm to 2.5 cm; and d) sample to collimator distance ranging from 0.01 cm to 6 cm. Dotted and dashed lines connecting the data points are depicted to highlight the variation trend of the relative sensitivity and position resolution, respectively. In b) and d), a linear fit to the position resolution values, following Eq. (3), is shown. Error bars corresponding to the calculated uncertainty are depicted.

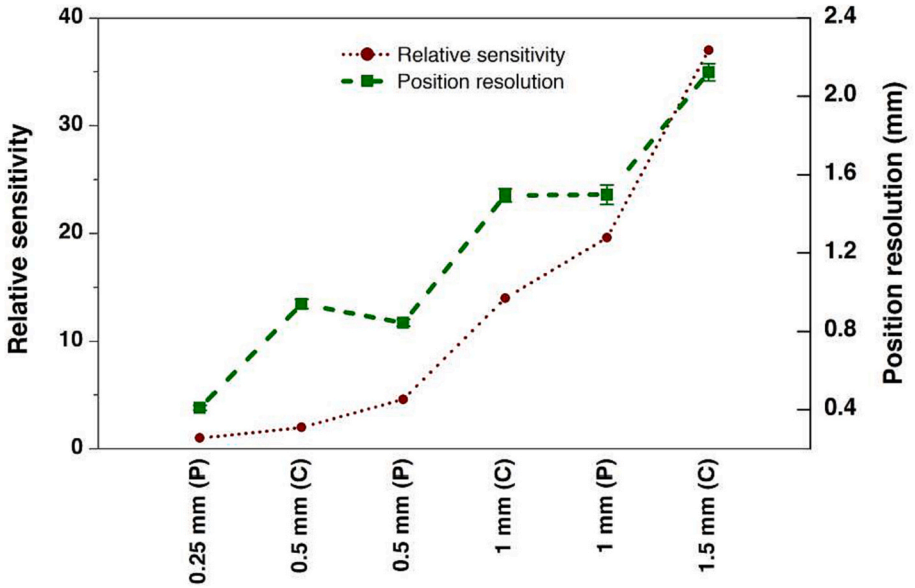

Fig. 9. Relative sensitivity and position resolution for pinhole apertures (P) and multi-hole collimators (C) with different hole diameters. Dashed and dotted lines are added connecting the relative sensitivity and position resolution data points, respectively, to highlight the trends. Error bars corresponding to the calculated uncertainty are depicted.

collimator with 1.5 mm holes, respectively.

It is interesting that the results obtained for multi-hole collimators with 0.5 mm and 1 mm holes show no improvement on the sensitivity when compared to the pinhole apertures of the same diameter. In these cases, the position resolution is approximately the same, as the diameter is the main component affecting it.

3.2. Experimental

Following the methodology presented in Section 2.2, the relative sensitivity of the FF-XRF spectrometer with the different optical components was experimentally determined. Results are shown in Fig. 10.

As expected, lower sensitivity was obtained when using pinhole apertures. The highest sensitivity was achieved for the Cu collimator, that yields a value approximately 45 times higher than with the smallest pinhole. This collimator has the lowest attenuation coefficient, which, combined with the small depth, increases the probability of photons passing through the material.

It is also interesting to note that the relative sensitivity obtained with the 1 mm pinhole is approximate to the one obtained with the 0.5 mm steel collimator.

Fig. 11 shows position resolution values for the FF-XRF spectrometer with different optical components. The expected values (green squares) were obtained using Eq. (1) and Eq. (3), assuming a detector intrinsic resolution of 1.5 mm FWHM; and the experimental values (dark red dots) were obtained following the methodology described in Section 2.2. The experimentally obtained values follow the expected trend – the position resolution improves with decreasing diameter and the best values are obtained with the pinhole apertures. It must be highlighted that the expected values are worse than the experimental ones, which possibly indicates that the assumed detector intrinsic resolution is underestimated.

Overall, better position resolution values were obtained when using pinhole apertures, with the best value obtained for the 0.3 mm pinhole aperture, 1.10 ± 0.02 mm FWHM. The worst value, 3.25 ± 0.09 mm FWHM, was obtained with the Pb collimator, as it presents the largest hole diameter (2 mm) and the largest collimator depth (4 cm). It was verified that the resolution for the steel collimators is approximately equal to the resolution obtained with pinhole apertures of the same diameter, which is expected as the resolution is mostly dependent on the hole diameter.

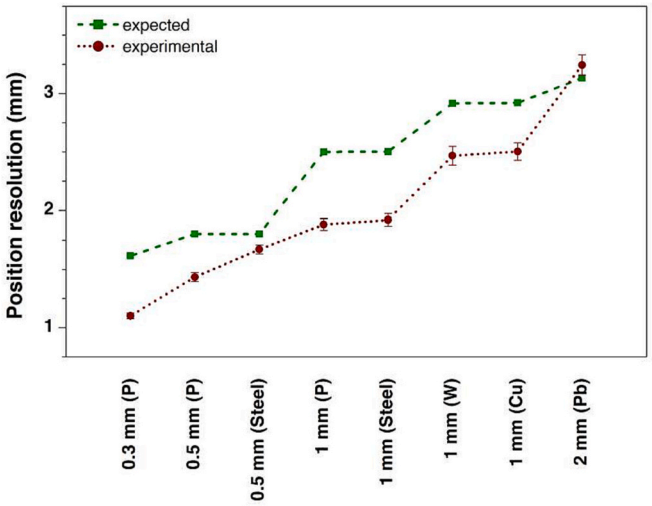

Fig. 11. Position resolution of the FF-XRF spectrometer with the different optical components – pinhole apertures (P) and multi-hole collimators of different materials. Green squares represent the expected values, and the red dots, the experimentally determined ones. To highlight the variation of the position resolution with the different optical components, dashed and dotted lines are depicted, connecting the expected and experimental data points, respectively. Error bars corresponding to the calculated uncertainty are depicted. (For interpretation of the references to colour in this figure legend, the reader is referred to the web version of this article.)

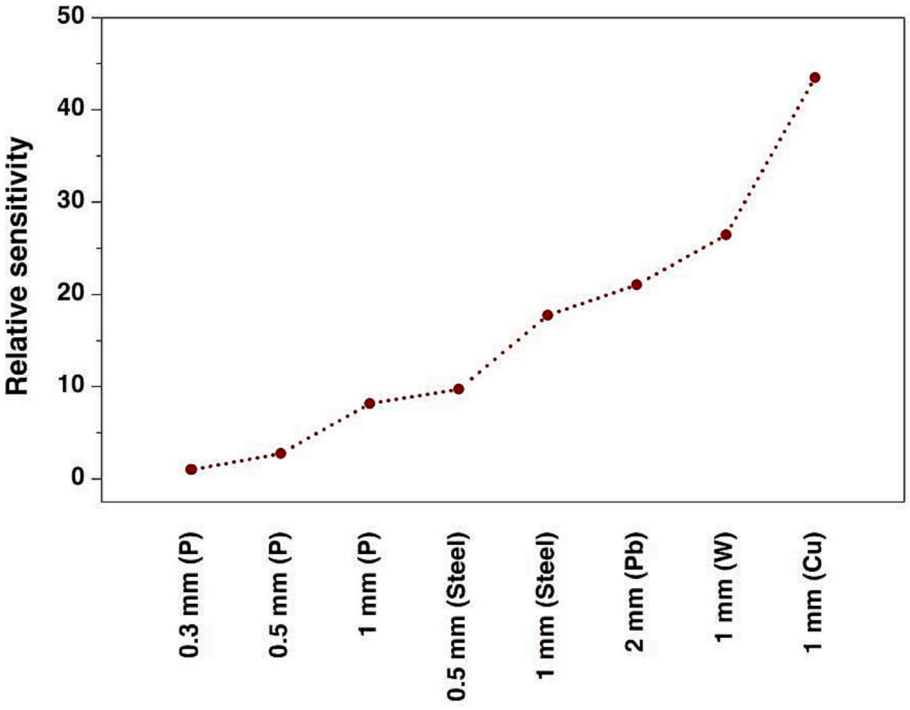

Fig. 10. Relative sensitivity of the FF-XRF spectrometer with the different optical components (pinhole apertures, P, and collimators). To highlight the increasing trend of the relative sensitivity, a dotted line connecting the data points is depicted.

3.3. Elemental maps of known samples

The imaging capability of different setups of the FF-XRF spectrometer was evaluated through the analysis of a combination of Fe and Cu samples. For these acquisitions, the X-ray tube was operated at 21 kV and 750 μA; the acquisitions with the pinhole apertures lasted 15 *min*, and with the collimators, 7 *min*. The elemental distributions were obtained by selecting the regions of interest, corresponding to the K fluorescence peaks of Fe and Cu, in the obtained EDXRF spectrum, as demonstrated in Fig. 12.

The Fe and Cu maps, and the combined elemental maps for each setup are shown in Fig. 13.

Qualitatively, the maps obtained with the pinhole apertures are better than those obtained with the collimators. This is expected as the use of pinholes yields the lowest position resolution values. Still, the use of the steel collimators resulted in elemental maps of good quality, with slightly better sensitivity. Moreover, when using collimators, we were able to obtain the same information in half the acquisition time. It can also be seen that contrary to the images obtained with the pinhole apertures, the ones obtained with the collimators have some shadows. This is a result of the relief of the sample, and of its positioning in respect to the collimator.

4. Conclusions

In this work, we have studied the performance of a full-field XRF spectrometer based on the 2D-THCOBRA detector with different optical components, namely pinhole apertures and multi-hole collimators. We have evaluated the relative sensitivity and the position resolution of different setups, to understand how they vary with the geometry of the optical components. To do so, we have simulated the spectrometer using GATE and conducted experimental acquisitions to determine the parameters.

We verified that the use of smaller pinholes limits the system sensitivity but allows better position resolution, while collimators with large holes and small septa lead to higher sensitivity, but negatively impact the system's position resolution. The best position resolution, 1.10 ± 0.02 mm FWHM, was achieved with a 0.3 mm diameter pinhole aperture, that also yielded the lowest relative sensitivity. Conversely, the Pb collimator with 2 mm hexagonal holes presented the worse position resolution value, 3.25 ± 0.09 mm FWHM. Regarding the sensitivity, the low attenuation coefficient and small depth of the Cu collimator with 1 mm circular holes, led to the best sensitivity – 50 times higher than the value achieved with the smaller pinhole aperture.

In this work, we have shown the applicability of multi-hole collimators for XRF imaging, and the results also emphasise the crucial trade-off between sensitivity and position resolution, showing how the optical component must be chosen accordingly to the desired application. One inherent disadvantage of multi-hole collimators must also be highlighted – magnification is no longer possible. Despite leading to lower sensitivities, pinhole apertures allow magnification by changing distances between the sample, optic component, and detector, which can be useful depending on the application. Converging hole collimators can also be used to produce magnified images of small samples, as well as multi-pinhole collimators. The latter have been extensively used in SPECT imaging of small animals [25], as high position resolution and increased sensitivity are achieved. Finally, we highlighted 3D printed collimators as a promising cost-effective solution for EDXRF system applications, that may allow us to explore different geometries and designs.

CRediT authorship contribution statement

P.M.S. Carvalho: Formal analysis, Investigation, Methodology, Writing – original draft, Writing – review & editing. **F.D. Leite:** Investigation, Writing – original draft, Writing – review & editing. **Gil Tavares:** Formal analysis, Investigation, Software. **P.M.M. Correia:** Software, Writing – review & editing. **J.M.M. Oliveira:** Funding acquisition, Resources, Writing – review & editing. **J.F.C.A. Veloso:** Conceptualization, Funding acquisition, Supervision. **A.L.M. Silva:** Conceptualization, Methodology, Supervision, Writing – review & editing.

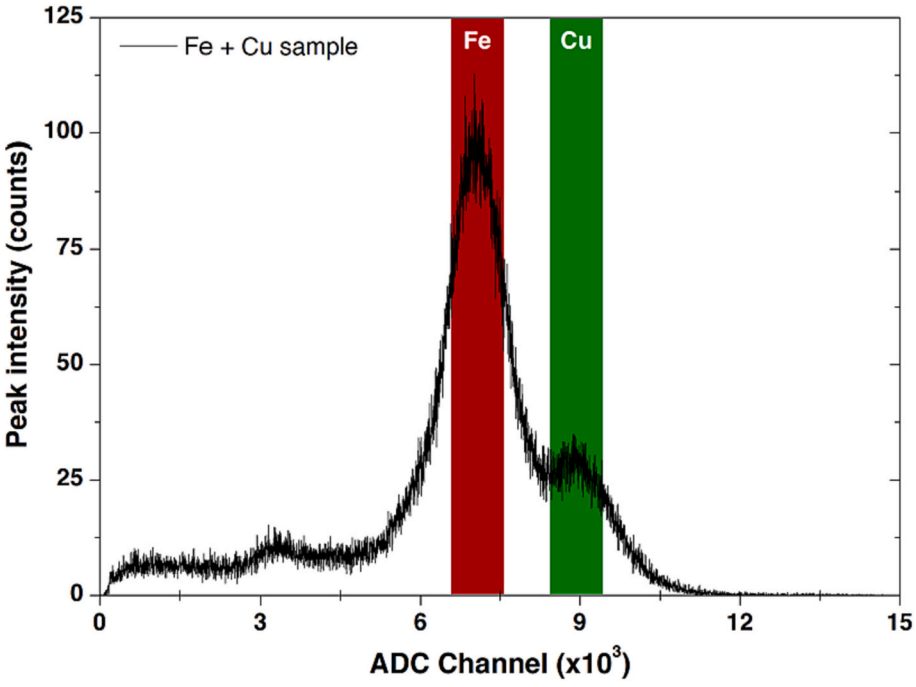

Fig. 12. EDXRF spectrum of an iron and copper sample, obtained with the FF-XRF spectrometer with a 0.5 mm pinhole aperture. The K fluorescence peak of Fe and Cu are highlighted in red and green, respectively. (For interpretation of the references to colour in this figure legend, the reader is referred to the web version of this article.)

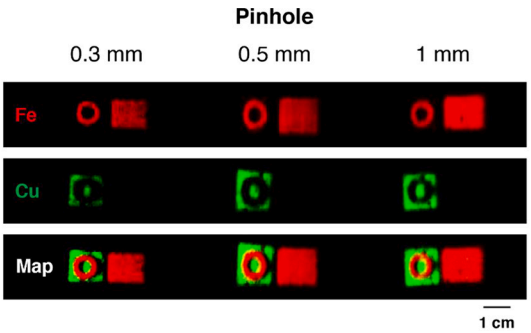

a)

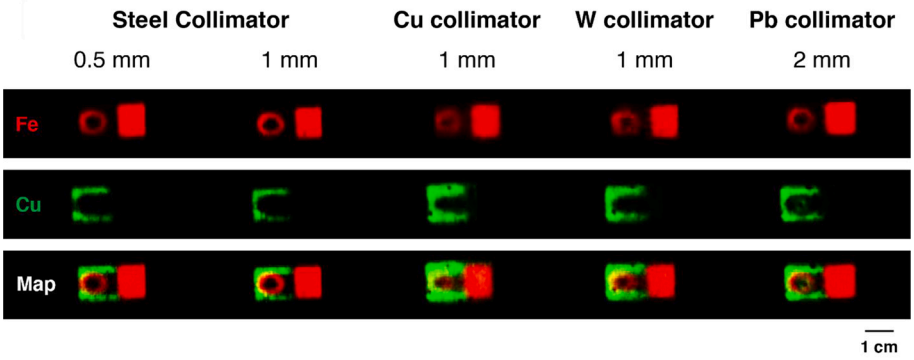

b)

Fig. 13. Elemental distribution maps of the known sample, obtained with the different tested optical components – a) pinholes, and b) multi-hole collimators.

Declaration of Competing Interest

None.

Data availability

Data will be made available on request.

Acknowledgments

This work was supported by project CERN/FIS-INS/0013/2021, by the European Union's Horizon 2020 research and innovation programme under grant agreement STRONG-2020 – No 824093, and by projects i3N (UIDB/50025/2020 and UIDP/50025/2020) and CICECO – Aveiro Institute of Materials (UIDB/50011/2020, UIDP/50011/2020 & LA/P/0006/2020), through the FCT/MCTES (PIDDAC).

The authors acknowledge Grupo Simoldes (Oliveira de Azeméis, Portugal), particularly Engenheiro João Vieira, for SLM manufacturing of the parallel multi-hole collimators used in this study.

References

[1] J.F.C.A. Veloso, A.L.M. Silva, Gaseous detectors for energy dispersive X-ray fluorescence analysis, Nucl. Instrum. Methods Phys. Res. A 878 (2018) 24–39, https://doi.org/10.1016/j.nima.2017.09.011.

[2] A.L.M. Silva, R. Figueroa, A. Jaramillo, M.L. Carvalho, J.F.C.A. Veloso, Performance of a gaseous detector based energy dispersive X-ray fluorescence imaging system: analysis of human teeth treated with dental amalgam, Spectrochim. Acta Part B At Spectrosc. 86 (2013) 115–122, https://doi.org/10.1016/j.sab.2013.03.005.

[3] A.L.M. Silva, M.L. Carvalho, K. Janssens, J.F.C.A. Veloso, A large area full-field EDXRF imaging system based on a THCOBRA gaseous detector, J. Anal. At. Spectrom. 30 (2015) 343–352, https://doi.org/10.1039/C4JA00301B.

[4] A.L.M. Silva, S. Cirino, M.L. Carvalho, M. Manso, S. Pessanha, C.D.R. Azevedo, L.F. N.D. Carramate, J.P. Santos, M. Guerra, J.F.C.A. Veloso, Elemental mapping in a contemporary miniature by full-field X-ray fluorescence imaging with gaseous detector vs. scanning X-ray fluorescence imaging with polycapillary optics, Spectrochim. Acta Part B At Spectrosc. 129 (2017) 1–7, https://doi.org/10.1016/j.sab.2016.12.006.

[5] P.M.S. Carvalho, F. Leite, A.L.M. Silva, S. Pessanha, M.L. Carvalho, J.F.C.A. Veloso, J.P. Santos, Elemental mapping of Portuguese ceramic pieces with a full-field XRF scanner based on a 2D-THCOBRA detector, Eur. Phys. J. Plus 136 (2021) 423, https://doi.org/10.1140/epjp/s13360-021-01422-y.

[6] F.D. Leite, P.M.S. Carvalho, R.G. Oliveira, M.C. Lopes, I. Domingues, P.M. M. Correia, L.F.N.D. Carramate, S. Pessanha, J.F.C.A. Veloso, A.L.M. Silva, Analysis of zebrafish contamination with heavy metals using a FF-XRF imaging system based on a MPGD, Spectrochim. Acta Part B At Spectrosc. 198 (2022), 106545, https://doi.org/10.1016/j.sab.2022.106545.

[7] A.L.M. da Silva, MPGDs Based Radiation Imaging Devices and Applications, PhD thesis,, Universidade de Aveiro, 2013.

[8] P.M.S. Carvalho, Energy Dispersive X-Ray Fluorescence Analysis Imaging — Development and Applications, PhD thesis,, Universidade NOVA de Lisboa, 2022, http://hdl.handle.net/10362/135615.

[9] J.T. Bushberg, J.A. Seibert, E.M. Leidholdt Jr., J.M. Boone, The Essential Physics of Medical Imaging, 3rd ed., Lippincott Williams & Wilkins, 2002.

[10] R. Accorsi, S.D. Metzler, Analytic determination of the resolution-equivalent effective diameter of a pinhole collimator, IEEE Trans. Med. Imaging 23 (2004) 750–763, https://doi.org/10.1109/TMI.2004.826951.

[11] K. Van Audenhaege, R. Van Holen, S. Vandenberghe, C. Vanhove, S.D. Metzler, S. C. Moore, Review of SPECT collimator selection, optimization, and fabrication for clinical and preclinical imaging, Med. Phys. 42 (2015) 4796–4813, https://doi.org/10.1118/1.4927061.

[12] U.D. Desai, L.E. Orwig, D. Clark, M. Appleby, in: J.H. Smith, J.M. Karam (Eds.), New fabrication methodology for fine-feature high-aspect-ratio structures made from high-Z materials, 1999, pp. 321–329, https://doi.org/10.1117/12.361236.

[13] O.V. Makarova, G. Yang, C.-M. Tang, D.C. Mancini, R. Divan, J. Yaeger, Fabrication of collimators for gamma-ray imaging, in: A.A. Snigirev, D.C. Mancini (Eds.), Design and Microfabrication of Novel X-Ray Optics II, SPIE, 2004, p. 126, https://doi.org/10.1117/12.563748.

[14] O.V. Makarova, G. Yang, P.T. Amstutz, C.M. Tang, Fabrication of antiscatter grids and collimators for X-ray and gamma-ray imaging by lithography and electroforming, Microsyst. Technol. (2008) 1613–1619, https://doi.org/10.1007/s00542-008-0558-7.

[15] Additive manufacturing — General principles — Fundamentals and vocabulary, 2021. https://www.iso.org/obp/ui/#iso:std:iso-astm:52900:ed-2:v1:en (accessed April 3, 2023).

[16] I. Gibson, D. Rosen, B. Stucker, M. Khorasani, Additive Manufacturing Technologies, Springer International Publishing, Cham, 2021, https://doi.org/10.1007/978-3-030-56127-7.

[17] D.W. Holdsworth, H.N. Nikolov, S.I. Pollmann, 3D-printed focused collimator for intra-operative gamma-ray detection, in: Medical Imaging 2017: Physics of Medical Imaging, SPIE, 2017, p. 101321L, https://doi.org/10.1117/12.2256051.

[18] K. Deprez, S. Vandenberghe, K. Van Audenhaege, J. Van Vaerenbergh, R. Van Holen, Rapid additive manufacturing of MR compatible multipinhole collimators with selective laser melting of tungsten powder, Med. Phys. 40 (2012), 012501, https://doi.org/10.1118/1.4769122.

[19] O.A. Mohamed, S.H. Masood, J.L. Bhowmik, Optimization of fused deposition modeling process parameters: a review of current research and future prospects, Adv. Manuf. 3 (2015) 42–53, https://doi.org/10.1007/s40436-014-0097-7.

[20] C.Y. Yap, C.K. Chua, Z.L. Dong, Z.H. Liu, D.Q. Zhang, L.E. Loh, S.L. Sing, Review of selective laser melting: materials and applications, Appl. Phys. Rev. 2 (2015), https://doi.org/10.1063/1.4935926.

[21] L.F.N.D. Carramate, A.L.M. Silva, C.D.R. Azevedo, D.S. Covita, J.F.C.A. Veloso, THCOBRA X-ray imagingdetector operating in Ne/CH_4, J. Instrum. 10 (2015), https://doi.org/10.1088/1748-0221/10/01/P01003.

[22] J.H. Hubbel, S.M. Seltzer, NIST Standard Reference Database 126, 2004, https://doi.org/10.18434/T4D01F.

[23] D.F.S. Ferreira, G. Miranda, F.J. Oliveira, J.M. Oliveira, Predictive models for an optimized fabrication of 18Ni300 maraging steel for moulding and tooling by selective laser melting, J. Manuf. Process. 70 (2021) 46–54, https://doi.org/10.1016/j.jmapro.2021.07.066.

[24] D. Sarrut, M. Bała, M. Bardiès, J. Bert, M. Chauvin, K. Chatzipapas, M. Dupont, A. Etxebeste, L.M. Fanchon, S. Jan, G. Kayal, A.S. Kirov, P. Kowalski, W. Krzemien, J. Labour, M. Lenz, G. Loudos, B. Mehadji, L. Ménard, C. Morel, P. Papadimitroulas, M. Rafecas, J. Salvadori, D. Seiter, M. Stockhoff, E. Testa, C. Trigila, U. Pietrzyk, S. Vandenberghe, M.-A. Verdier, D. Visvikis, K. Ziemons, M. Zvolský, E. Roncali, Advanced Monte Carlo simulations of emission tomography imaging systems with GATE, Phys. Med. Biol. 66 (2021) 10TR03, https://doi.org/10.1088/1361-6560/abf276.

[25] J.P. Janssen, J.V. Hoffmann, T. Kanno, N. Nose, J.P. Grunz, M. Onoguchi, X. Chen, C. Lapa, A.K. Buck, T. Higuchi, Capabilities of multi-pinhole SPECT with two stationary detectors for in vivo rat imaging, Sci. Rep. 10 (2020), https://doi.org/10.1038/s41598-020-75696-0.